CHEMISTRY OF MATERIALS

Open Access



pubs.acs.org/cm

Article

# Disorder in the Antifluorite Sulfide Cathode: $Li_{1.7}Cu_{0.15}S_2$

Akira Miura,* Yi-Ting Cheng, Takenaka Masahiro, Yusuke Nambu, Shunsuke Sasaki, Masanori Nagao, Takato Mitsudome, Yuta Fujii, Kiyoharu Tadanaga, Nobuya Machida, and Christopher J. Bartel*

Cite This: *Chem. Mater.* 2025, 37, 8521−8528

Read Online

ACCESS | Metrics & More | Article Recommendations | Supporting Information

**ABSTRACT:** Cation and anion substitutions in $Li_2S$ have improved their performance as high-capacity cathodes, but electron and ion transport in solid solutions of $Li_2S$ have not been fully understood due to intricate site disorder within the antifluorite structure. Herein, neutron diffraction identified a unique disordered structure of Cu-substituted $Li_2S$ ($Li_{1.7}Cu_{0.15}S$) within an antifluorite framework where Cu occupies an octahedral site in addition to the canonical tetrahedral one. This disorder leads to partial sulfur oxidation and facilitates $Li^+$ transport, as revealed by X-ray absorption, impedance, and magnetic measurements. Density functional theory calculations support the entropically stabilized nature of this disordered structure and shed insight on the influence of Cu substitution on electronic structure, vacancy formation, and ion transport. The proposed dual-site occupation suggests a mechanism for the improved performance of $Li_2S$-based cathodes with cation substitutions.

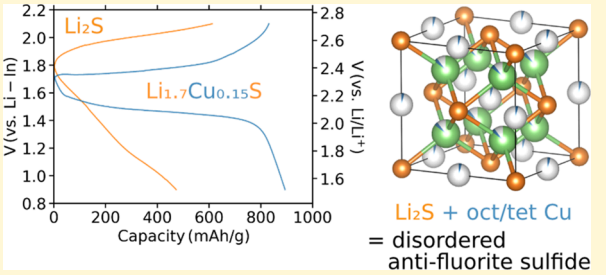




## INTRODUCTION

Increasing the energy density of all-solid-state batteries is a pressing issue for improving energy storage technologies, and developing high-capacity cathode materials is essential. Disordered rocksalt oxide (and oxyfluoride) cathodes (DRX) have garnered attention as high-capacity cathode materials[1,2] and ion conductors[3] and are composed of a face-centered-cubic (fcc) arrangement of anions and cations, where the octahedral cation site hosts significant disorder among Li and multivalent transition metals. DRX cathodes exhibit topotactic reactions, which offer the advantage of good cycling stability owing to minimal structural changes. On the other hand, $Li_2S$ has an antifluorite structure composed of an fcc anion (sulfide) framework with Li occupying the tetrahedral interstitial sites and is a high-capacity conversion cathode material with a theoretical capacity of 1167 mA h $g^{-1}$. This cathode utilizes conversion reactions[4] in contrast to the topotactic reactions that sustain the structural framework. When combined with sulfide solid electrolytes like $Li_3PS_4$, $Li_2S$ has been reported to exhibit a high capacity without dissolution of sulfur upon cycling.[5] However, the low electronic and ionic conductivities of $Li_2S$ present challenges for high-rate performance and long-term stability.

One strategy for enhancing ionic conductivity is to produce a solid solution of $Li_2S$ with lithium halides, such as LiCl, LiBr, and LiI.[6−10] $Li_2S$−LiI solid solutions, in particular, exhibit high ionic conductivity, likely due to the formation of LiI-rich domains that create Li ion conduction pathways.[8] The increase in lattice constants is also thought to contribute to the expansion of ion conduction pathways. Combining transition metals with $Li_2S$ is another effective strategy. In addition to using transition metal sulfides,[10−16] solid solutions of $Li_2S$ with other metal dopants have been reported.[17,18] Co-doping with Cu, O, and I has been reported to further enhance ionic conductivity and weaken the Li−S bond, promoting redox reactions.[9,10]

However, there is a limited understanding of the structure of these mixed-cation materials since most prior crystallographic analyses focused mostly on observing changes in the lattice constants via X-ray diffraction (XRD) along with compositional analysis.[9,18] While it is true that conversion materials undergo significant phase transformations upon cycling, the structure of the initial, as-synthesized material, is often critical for determining the kinetics and reversibility of the resulting phase transformations.[19] A fundamental understanding of structure and cation (dis)order is lacking and would help enable the rational design of doped $Li_2S$ cathode materials.

In this study, we synthesize and characterize $Li_{2-2x}Cu_xS$ electrodes in all-solid-state batteries (ASSBs) with improved electronic and ionic transport. Further, we use XRD and neutron diffraction (ND) along with density functional theory (DFT) calculations to resolve the structure of the synthesized materials. Contrary to the simple antifluorite structure assumed previously, our results indicate a mixed occupation of $Cu^+$ on the tetrahedral cation sites as well as (rocksalt-like) octahedral

Received: May 28, 2025
Revised: October 10, 2025
Accepted: October 13, 2025
Published: October 31, 2025

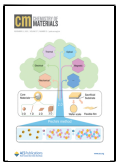

interstitial sites in the antifluorite structure. This interesting hybrid of antifluorite and rocksalt structures (coined "disordered antifluorite sulfide" or DAFS) is found to be entropically stabilized and accessed via mobile $Li^+$ ions.

## RESULTS AND DISCUSSION

In Figure 1a, we show the XRD patterns of $Li_{2-2x}Cu_xS$ phases synthesized at several compositions. All the peaks are indexed

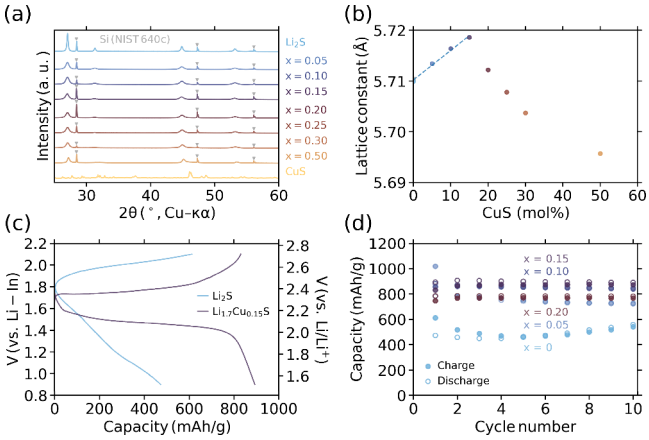


**Figure 1.** XRD patterns and lattice parameters of $Li_{2-2x}Cu_xS$ electrodes and their discharge−charge properties using $Li_3PS_4$−LiI electrolytes. For all panels, $x$ refers to the fraction of CuS in the $Li_{2-2x}Cu_xS$ solid solution. (a) XRD patterns of $Li_{2-2x}Cu_xS$ solid solution. Gray triangles indicate the inner standard of Si. (b) Lattice parameters of $Li_{2-2x}Cu_xS$. The dashed blue line indicates nearly linear initial expansion of the structure with CuS substitution before a nonlinear change at higher CuS concentrations. (c) Discharge−charge profile of $Li_{1.7}Cu_{0.15}S$ ($x$ = 0.15) and $Li_2S$ electrodes operated in ASSBs using sulfide solid electrolytes. (d) Capacity of $Li_{2-2x}Cu_xS$ electrode in ASSBs.

as a cubic phase, with the most prominent peaks aligning with pristine $Li_2S$. For $x$ > 0.20, the peaks exhibit shoulders toward higher angles (~45°), suggesting phase separation or a possible impurity phase. In Figure 1b, we show the trend in lattice parameters from these XRD patterns. The lattice parameter was found to increase steadily up to $x$ = 0.15, before dropping significantly upon further incorporation of Cu. This lattice parameter decrease coincides with the appearance of the impurity peaks in Figure 1a, so it may not be associated with lattice contraction in the $Li_{2-2x}Cu_xS$ phase. In Figure 1c, we show the first discharge−charge cycle for $Li_2S$ ($x$ = 0) and $Li_{1.7}Cu_{0.15}S$ ($x$ = 0.15) as cathode materials under a current density of 6.4 $\mu$A $cm^{-2}$ at 60 °C against an In anode with $Li_3PS_4$ solid electrolyte. The incorporation of Cu nearly doubles the observed capacity. In Figure 1d, we show that this Cu composition leads to the highest reversible capacity over 10 cycles, and the capacity was further demonstrated to be 890 mA h $g^{-1}$ over 40 cycles (Figure S1). Ionic and electronic conductivities measured by direct current measurement with electronic and ionic blocking for this same composition were $3.9 \times 10^{-8}$ and $4.7 \times 10^{-8}$ S $cm^{-1}$ for $Li_{1.7}Cu_{0.15}S$ (Figure S2), significantly higher than those of $Li_2S$ (≈$10^{-11}$ S $cm^{-1}$). Subsequent discussion focuses on this $x$ = 0.15 phase to understand the electrochemical performance through the crystal and electronic structure of this material.

To elucidate the crystal structure of the optimal $Li_{1.7}Cu_{0.15}S$ composition, we performed synchrotron X-ray diffraction (SXRD) and neutron diffraction (ND), as shown in Figure 2a. The diffraction patterns indicates a single-phase material

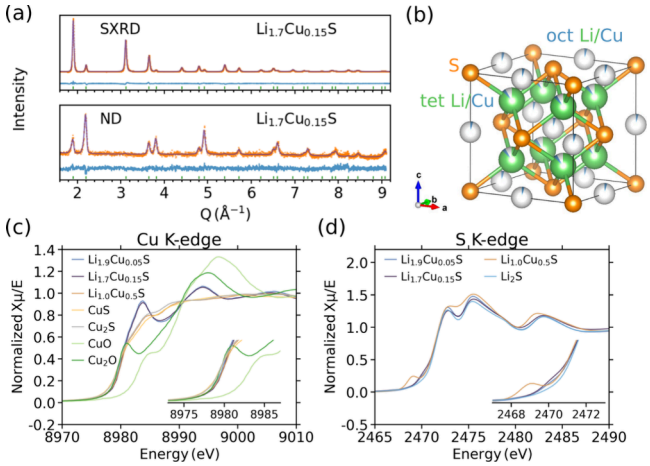


**Figure 2.** Structural analysis of $Li_{1.7}Cu_{0.15}S$ electrode. (a) SXRD pattern (top) and ND pattern of $Li_{1.7}Cu_{0.15}S$ (bottom). The reference ticks colored in green correspond with Bragg peak positions. (b) Proposed crystal structure of $Li_{1.7}Cu_{0.15}S$. Blue, green, orange, and gray refer to copper, lithium, sulfur, and vacancy occupations, respectively. (c) Cu K-edge absorption of pristine $Li_{2-2x}Cu_xS$. (d) S K-edge absorption of pristine $Li_{2-2x}Cu_xS$.

with a face-centered S sublattice and tetrahedral Li, consistent with the antifluorite structure of $Li_2S$. However, ND reveals that Cu occupies both tetrahedral and interstitial octahedral sites, highlighted by the significant difference in bound coherent scattering lengths between Li (−1.90 fm) and Cu (7.718 fm), as shown in Table S1.[20] These octahedral sites in the face-centered sulfide framework are the cation sites in the normal rocksalt structure. The proposed crystal structure is shown in Figure 2b and depicts the partial occupation of Cu on both the antifluorite tetrahedral sites and the nominal rocksalt octahedral sites. The refinement details are shown in Table 1.

**Table 1. Refined Crystallographic Parameters from Combined Rietveld Analysis of SXRD and ND for $Li_{1.7}Cu_{0.15}S$, Measured at ca. 300 K[a]**

| site | Wyckoff position | $x$ | $y$ | $z$ | occupancy | $B$ (Å$^2$) |
|---|---|---|---|---|---|---|
| Li1 | 8$c$ | 1/4 | 1/4 | 1/4 | 0.821(12) | 1.09(6) |
| Cu1 | 8$c$ | 1/4 | 1/4 | 1/4 | 0.053(10) | =Li1 |
| Li2 | 4$b$ | 1/2 | 1/2 | 1/2 | 0.020(5) | =Li1 |
| Cu2 | 4$b$ | 1/2 | 1/2 | 1/2 | 0.054(12) | =Li1 |
| S | 4$a$ | 0 | 0 | 0 | 1 | 0.41(4) |

[a]Crystal system: cubic. Space group: $Fm\bar{3}m$. Lattice parameter: $a$ = 5.7096(3) Å. Reliability factors: $R_{wp}$ = 2.31%, $R_p$ = 1.80%, and GoF = 0.39 for the SXRD. $R_{wp}$ = 8.81%, $R_p$ = 6.59%, and GoF = 1.34 for ND.

The final composition determined by Rietveld refinement is $Li_{1.66(2)}Cu_{0.16(2)}S$, which is in agreement with the targeted nominal composition of $Li_{1.7}Cu_{0.15}S$. ICP measurement showed the molar ratio of Cu/Li as 0.078, which is also close to the nominal ratio of 0.088. Due to this mixed occurrence of antifluorite and octahedral cation sites, we term this structure disordered antifluorite sulfide. This structure is similar to full Heusler alloys[21] and $BiF_3$,[22] but has not been explored yet in sulfides.


https://doi.org/10.1021/acs.chemmater.5c01328
Chem. Mater. 2025, 37, 8521−8528

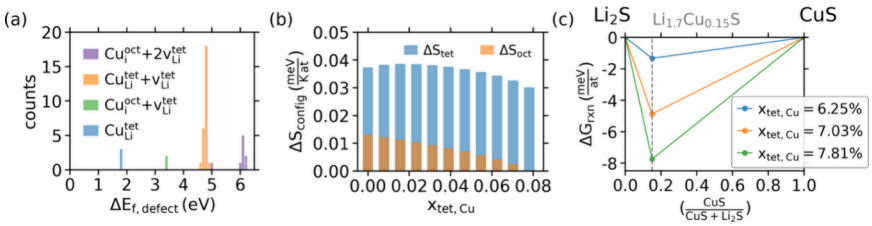


**Figure 3.** (a) Distribution of defect formation energies for four different Cu defects: tetrahedral/octahedral monovalent/divalent Cu. (b) Variation in total configurational entropy $\Delta S_{config}$ with the tetrahedral Cu ratio in $Li_{1.7}Cu_{0.15}S_2$. (c) Reaction free energy at 300 K, $\Delta G_{rxn}$, to form $Li_{1.7}Cu_{0.15}S_2$ with respect to the $\frac{CuS}{CuS+Li_2S}$ ratio considering various tetrahedral Cu occupancies ($x_{tet,Cu}$). The $x$-axis denotes the mixing ratio between $Li_2S$ $\left(\frac{CuS}{CuS+Li_2S}=0\right)$ and CuS $\left(\frac{CuS}{CuS+Li_2S}=1\right)$, and the $y$-axis shows the reaction free energy $\Delta G_{rxn}$ to form $Li_{1.7}Cu_{0.15}S_2$ with respect to the end-members $Li_2S$ and CuS.

To understand the electronic structure of Cu in this material, we used X-ray absorption fine structure (XAFS) measurements as shown in Figure 2c,d. Beginning with the Cu K-edge (Figure 2c), we first observe that the rising edge energy of $Li_{2-2x}Cu_xS$ ($x$ = 0.05, 0.15, 0.5) is more consistent with $Cu_2O$ ($Cu^+$) than CuO ($Cu^{2+}$). The absence of $Cu^{2+}$ species is commonly observed in Cu−S compounds, regardless of the coordination environment around Cu cations.[23] For instance, CuS Covellite was formally believed to contain $Cu^{2+}$ but later identified as cuprous ($Cu^+$).[24] In general, $Cu^{2+/+}$ redox couples are situated below the top of the S 3p band, leading to preferential oxidation of sulfur anions. The oxidation of S states may condense into $(S_2)^{2-}$ dimers[25,26] or delocalize as itinerant holes through strong hybridization with Cu 3d bands.[27−29] Accordingly, our XAFS measurements at the S K-edge showed the gradual emergence of the pre-edge feature at around 2470 eV. This pre-edge feature can be assigned to the S 1s → 3p dipolar transition indicative of hole formation on S 3sp bands.[30] These observations are consistent with the redox competition between $Cu^{2+/+}$ couples and sulfur anions; cation vacancies in the $Li_2S$−CuS solid solution likely create holes near the valence band maximum with mainly S 3sp character. Our magnetometry measurements of the $Li_2S$−CuS solid solution (Figure S3) revealed that their molar susceptibilities were characterized mainly by temperature-independent paramagnetism. If $Li_{2-2x}Cu_xS$ carries only localized spins with their divalent $Cu^{2+}$ ($d^9$) cations, its spin-only effective moment of 1.73 $\mu_B$ should lead to temperature-dependent paramagnetism with Curie constants around 0.375 emu K $mol^{-1}$ per Cu. The observed Curie constants were far smaller than this value expected for the fully localized electrons. In contrast, their temperature-independent susceptibilities amounted to the order of $10^{-2}$ to $10^{-3}$ emu $mol^{-1}$ per Cu, which are larger by two or three orders of magnitude than typical Pauli paramagnets such as alkali metals.[31] Such a strong temperature-independent contribution is commonly observed from heavily hole-doped semiconductors based on copper sulfides, reflecting Pauli paramagnetism of their itinerant carriers.[32] Therefore, the created sp holes can be considered itinerant through hybridization with Cu 3d/4s allowing enhanced electron conductivity in the solid solutions.

To better understand the nature of Cu substitution into $Li_2S$, we performed density functional theory (DFT) calculations using the PBE functional.[33] Starting with dilute defect calculations, in Figure 3a, we show the formation energy distribution for various Cu defect configurations: (1) tetrahedral monovalent Cu ($Cu_{Li}$, directly substituting Li with Cu), (2) octahedral monovalent Cu ($Cu_i + v_{Li}$, requiring a Li vacancy for charge-balance), (3) tetrahedral divalent Cu ($Cu_{Li} + v_{Li}$, also requiring a Li vacancy), and (4) octahedral divalent Cu ($Cu_i + 2\ v_{Li}$, requiring two Li vacancies). The energy trends indicate that Cu preferentially occupies tetrahedral sites in a monovalent state, while octahedral and divalent configurations are energetically unfavorable due to the additional Li vacancies required for charge-balance. These findings are consistent with the Cu K-edge spectra shown in Figure 2c.

Following these dilute defect calculations, we extended our investigation to the refined composition: $Li_{1.7}Cu_{0.15}S$. Based on the XRD/ND analysis, we presume that Li can only occupy tetrahedral sites while Cu can occupy either tetrahedral or octahedral sites. Compared with the antifluorite composition ($Li_2S$), this composition is cation deficient (cation:anion ratio of 1.85:1), so vacancies can also appear on both the tetrahedral and octahedral sites. In the subsequent analysis, we refer to $x_{tet,Cu}$ as the occupation of Cu on the tetrahedral site. Since there are two tetrahedral sites and one octahedral site, at the $x$ = 0.15 composition, $x_{oct,Cu} = 0.15 - 2x_{tet,Cu}$, and the concentration of tetrahedral vacancies, $x_{tet,vac} = 0.15 - x_{tet,Cu}$ (since $x_{tet,Li} = 0.85$). In our DFT calculations, we approximate the $x$ = 0.15 composition as $Li_{110}Cu_{10}S_{64}$ to be amenable to a 4 × 4 × 4 supercell of $Li_2S$ (equivalent to a 4 × 2 × 2 supercell of the refined structure shown in Figure 2b).

First, we estimated the effect of octahedral Cu occupation on the total configurational entropy of the system assuming ideal mixing of Li/Cu/vacancy on the tetrahedral site and ideal mixing of Cu/vacancy on the octahedral site. As shown in Figure 3b, mixed occupation of Cu on the tetrahedral and octahedral sites maximizes the configurational entropy, though the changes are small across various occupations. We attempted to enumerate many ordered configurations at each of the tetrahedral Cu occupations shown in Figure 3b but found that octahedral Cu frequently relaxed back to neighboring (vacant) tetrahedral sites during geometry relaxation with DFT. As such, we only report energies associated with tetrahedral Cu occupation ≥6.25% where we were able to relax structures with octahedral Cu. The free energy, $\Delta G_{rxn}$, of forming $Li_{1.7}Cu_{0.15}S$ from ~0.85 $Li_2S$ + ~0.15 CuS, is shown in Figure 3c (the exact reaction is reported and discussed in Methods), where the reaction enthalpy is taken to be the DFT reaction energy, the reaction entropy is taken to be the configurational entropy estimated with an ideal solution model, and the temperature is taken to be 300 K. The formation of structures with mixed tetrahedral/octahedral Cu


https://doi.org/10.1021/acs.chemmater.5c01328
Chem. Mater. 2025, 37, 8521−8528

was found to be favorable, but 7.8% tetrahedral Cu and 0% octahedral Cu was found to have the most negative $\Delta G_{rxn}$. In comparison, the ND/XRD refinement indicates 5.5% of tetrahedral sites are occupied by Cu. The observed ionic conductivity of these samples by impedance suggests that dynamic site evolution may play a role in the observed occupancies.

Ab initio molecular dynamics (AIMD) and CHGNet MD simulations[34] were conducted to examine the dynamics of Cu and Li starting from the DFT-relaxed $Li_{1.7}Cu_{0.15}S_2$ structure with 7.8% tetrahedral Cu. The temperature was set to 800 K to facilitate sufficient dynamics on a reasonable simulation time scale. In Figure 4a, we show the coordination number (CN)

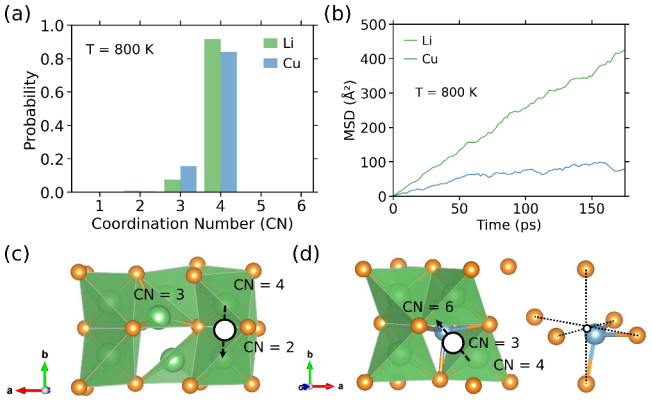


**Figure 4.** (a) Coordination number (CN) distribution of Li and Cu cations in $Li_{1.7}Cu_{0.15}S$, computed by AIMD at 800 K for 10 ps. (b) Mean square displacement (MSD) of Li and Cu showing the fast diffusion of Li compared to Cu obtained from CHGNet MD simulations at 800 K. The migration pathways of (c) Li and (d) Cu (left) from AIMD snapshots illustrate the variation in CN during cation diffusion. When Li cations migrate from one tetrahedral site to an empty edge-sharing tetrahedral site (Li vacancy), the CN transitions sequentially from 4 (tetrahedra center) to 3 (tetrahedral face), then to 2 (tetrahedral edge), before returning to CN = 3 and CN = 4. The migration pathway of Cu cations involves movement from a tetrahedral site to a face-sharing octahedral site, during which the CN transitions from 4 (initial tetrahedral site) to 3 (tetrahedral face), and finally to 6 (octahedral site). On the right side of (d), the distortion of the Cu cation from the octahedral center is shown, resulting in a CN of 3 rather than 6.

distribution of Li and Cu cations during the 0.5 to 10.5 ps AIMD simulation period. Li and Cu are both found to be primarily 4-fold coordinated (90% for Li; 85% for Cu). Both cations are also assigned to CN = 3 environments with non-negligible probabilities (10% for Li, 15% for Cu). Li was found to have significantly more mobility than Cu based on the observed mean square displacement (MSD) evolution calculated with CHGNet MD for an extended simulation time of 175 ps (following 25 ps of equilibration) as shown in Figure 4b. This enhanced Li mobility is likely associated with the significant tetrahedral vacancy concentration in the disordered antifluorite structure. The 3-fold coordination environments observed for Li are consistent with the migration pathway between adjacent tetrahedral sites in the antifluorite structure (Figure 4c). Alternatively, Cu was not found to exhibit significant mobility in this structure but was still found to exhibit significant 3-fold coordination environments. By inspection of the structures evolving during the AIMD simulation, we ascribe these CN = 3 environments to the dynamic occupation of Cu in distorted octahedral sites as shown in Figure 4d.

It should be noted that the 3-fold-coordinated Cu found in our simulations does not contradict the average octahedral coordination observed experimentally. Experimental diffraction probes the long-range average structure, showing a 6-fold-coordinated Cu in a rocksalt-type lattice. On the other hand, MD simulations can reveal the short-range local coordination. The simulation results with 3-fold-coordinated Cu provide an insight not visible from the average structure and are consistent with the known chemistry of Cu. Thus, a key finding of this research is that while the average structure is rocksalt-type, a unique local coordination environment is formed dynamically.

To complement the XAFS characterization of the Cu/S electronic structure in these disordered antifluorite structures, we calculated the electronic density of states and Bader charges using the r$^2$SCAN functional.[35] In Figure 5a, we report the calculated Bader charge distribution for S ions surrounding tetrahedral or octahedral Cu, as determined by DFT for $Li_{1.7}Cu_{0.15}S$ with Cu occupying 6.25% of the tetrahedral sites and 3.1% of the octahedral sites. S anions near octahedral Cu exhibit a more covalent character (less negative Bader charge value of $\approx -1.38$) compared to those around tetrahedral Cu ($-1.50$), consistent with a more covalent nature of the Cu−S bond in octahedral Cu. Additionally, when S anions are adjacent to Li vacancies, they exhibit a more ionic character (Bader charge $< -1.64$). In Figure 5b, we present the average Bader charge values for Li, tetrahedral and octahedral Cu, and S ions. Compared to the parent compound $Li_2S$, the average Bader charge for Li remains unchanged (approximately 0.86), while the charge on S increases from $-1.72$ to $-1.56$. This finding suggests that the Bader charge of Li is unaffected by the Cu substitution, whereas S anions undergo partial oxidation, consistent with the preference for $Cu^+$ in sulfides. Octahedral Cu cations hold a lower average Bader charge (0.44) compared to tetrahedral Cu (0.50), reflecting a slightly more covalent character. The introduction of both interstitial (octahedral) and substitutional (tetrahedral) Cu defects results in local oxidation of nearby S anions. In Figure 5c, we show the density of states (DOS) and crystal orbital Hamilton population (COHP) of $Li_{1.7}Cu_{0.15}S$, highlighting the bonding/antibonding environments between cation and S states. $-$COHP $> 0$ values denote bonding interactions, while $-$COHP $< 0$ corresponds to antibonding states at a given energy. The states near the Fermi level are dominated by S states, consistent with the redox couple picture where Cu states sit below the anion S 3p band. Partial oxidation of S into the conduction band aligns with the observed increase in S Bader charges and the emerging pre-edge feature in XAFS. COHP analysis reveals strong Cu−S antibonding interactions, indicating high Cu−S covalency. From the molecular orbital perspective, tetrahedral $Cu^{2+/+}$ in a sulfur ligand field features frontier orbitals with strong antibonding character arising from interaction with S 3p states, as shown in Figure 5d. These findings suggest that S holes formed during CuS incorporation are stabilized by Cu−S hybridization.

When considering the generalizability of the solid solution formation mechanism revealed in this study to other transition metal systems, the unique chemical nature of Cu must be taken into account. Cu is distinct from many other transition metals due to its often monovalent nature and preference for low coordination numbers, such as trigonal planar.[36,37] Therefore, the extensive solid solution range observed in the $Li_{2-2x}Cu_xS$


https://doi.org/10.1021/acs.chemmater.5c01328
Chem. Mater. 2025, 37, 8521−8528

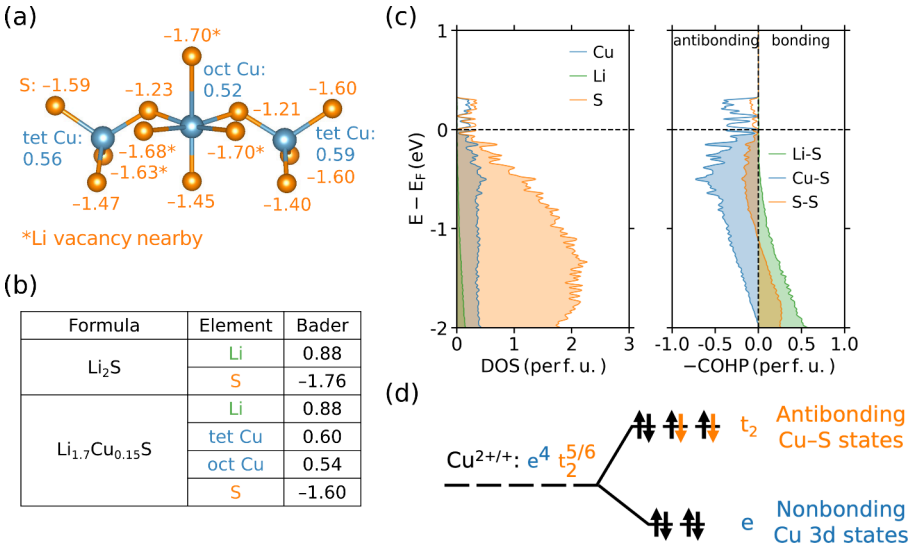


| Formula | Element | Bader |
|---|---|---|
| $Li_2S$ | Li | 0.88 |
| | S | -1.76 |
| $Li_{1.7}Cu_{0.15}S$ | Li | 0.88 |
| | tet Cu | 0.60 |
| | oct Cu | 0.54 |
| | S | -1.60 |

**Figure 5.** (a) Bader charge distribution on tetrahedral Cu, octahedral Cu, and S in $Li_{1.7}Cu_{0.15}S$. Note: there are Li vacancies near the S anions. (b) Average Bader charges on each ion (Li, octahedral Cu, tetrahedral Cu cations, and S anions) in $Li_{1.7}Cu_{0.15}S$. (c) Element-projected DOS and COHP for $Li_{1.7}Cu_{0.15}S$. (d) Crystal orbital picture of tetrahedral $Cu^{2+/+}$ in a sulfur ligand field.

system is likely attributable to this special characteristic of Cu. Determining whether a similar phenomenon could occur with other transition metals or halides requires careful consideration of their respective coordination chemistries and preferred oxidation states.

## CONCLUSIONS

This work reveals that the significantly enhanced electrochemical performance of $Li_2S$−CuS solid solutions—delivering a reversible capacity of 890 mA h $g^{-1}$ over 40 cycles—originates from a novel structural motif, which we term the "disordered antifluorite sulfide" (DAFS). A synergistic combination of multimodal experimental analyses and first-principles calculations demonstrates that, contrary to a simple substitution model, monovalent copper, $Cu^+$, occupies both the canonical tetrahedral sites of the antifluorite framework and previously unobserved interstitial octahedral sites. This dual-site occupation, creating a unique hybrid of antifluorite and rocksalt-like features, is deemed the origin of the material's superior properties as a high-capacity conversion cathode for all-solid-state batteries, enhancing both electronic and ionic conductivity compared with $Li_2S$. The presence of $Cu^+$ induces partial oxidation of the sulfur framework, creating itinerant holes with strong S 3p−Cu 3d hybridization that significantly boost electronic conductivity, as confirmed by X-ray absorption spectroscopy and magnetic measurements. Concurrently, the formation of the DAFS structure generates a high concentration of tetrahedral Li vacancies, which establishes an interconnected network for rapid $Li^+$ transport. This study establishes a powerful approach to enhance high-capacity conversion cathodes by engineering cation disorder across multiple crystallographic sites. This strategy provides a foundational understanding of the role of Cu in improving the performance of $Li_2S$-based cathode materials in the context of next-generation, high-energy all-solid-state lithium batteries.

## METHODS

$Li_2S$−CuS was synthesized by ball-milling techniques. $Li_2S$ (Mitsuwa, 99.9%) and CuS (Fuji-Wako, 99.5%) were used as the starting materials. $Li_2S$ and CuS were mixed in stoichiometric amounts by an agate mortar for 30−40 min in an Ar-filled glovebox. The mixtures were sealed in zirconia pots and mixed with 3 mm and 100 mm diameter zirconia balls for 40 h. X-ray diffraction (XRD) patterns of the samples were recorded using an X-ray diffractometer (MiniFlex600) with CuK$\alpha$ radiation source. The diffraction was measured by synchrotron X-ray sources at the BL13XU beamline of SPring-8 (2024B1777)[38] and neutron at a wavelength of 1.34177 Å using HERMES at JRR-3 at the Japan Atomic Energy Agency.[39] The crystal structure was analyzed by TOPAS.[40] The Cu/Li ratio was measured by inductively coupled plasma optical emission spectroscopy (ICP-OES ICPE-9000). XAFS of the Cu−K edge was measured at BL01B1 beamline of SPring-8 (2024B1602) and that of the S−K edge was acquired at BL6N1 beamline at the Aichi synchrotron center (202404113). Magnetic properties were measured with a vibrating sample magnetometer using a physical property measurement system (PPMS DynaCool).

The ionic conductivity was determined using a DC two-probe method with electron-blocking electrodes. A densified sample pellet was placed in a symmetric cell (Li|blocking layer|sample|blocking layer|Li). The blocking layers consisted of a 40LiI·60$Li_3PS_4$ (mol %) glass ($\sigma_{Li+}$ = 2 × $10^{-3}$ S·$cm^{-1}$ at 298 K) to prevent electron transport. Upon applying a constant DC voltage (0.5−1.5 V), the resulting steady-state current, carried exclusively by $Li^+$ ions, was measured to calculate the ionic conductivity. The electronic conductivity was measured separately via a DC polarization method using an ion-blocking cell configuration (Ni|sample|Ni). The sample was sandwiched between two nickel rods that served as $Li^+$ ion-blocking electrodes. When a DC voltage of 0.5−1.5 V was applied, the current decayed and reached a steady-state value after ∼30 min. This residual current was considered purely electronic, as the ionic flow was blocked, and was used to determine the electronic conductivity.

The all-solid-state batteries containing the obtained powders as the cathode materials were constructed according to previous reports[8] to investigate the electrochemical behavior of the samples. $Li_3PS_4$ glass powders and In sheets were used as the solid electrolyte and the anode materials, respectively. The composite cathodes were prepared by mixing the obtained powders, $Li_3PS_4$ glass powders, and vapor-grown carbon fibers (VGCF, Showa Denko) with the weight ratio of 50:40:10 in an agate mortar. The composites were used as the cathode layer (10 mg). The battery cycling tests were carried out by using a charge−discharge measuring device (Scribner Associates, 580 battery-type system) under the current density of 6.4 $\mu$A $cm^{-2}$ at 60 °C.


https://doi.org/10.1021/acs.chemmater.5c01328
Chem. Mater. 2025, 37, 8521−8528

Density functional theory (DFT) calculations were performed using the Vienna Ab Initio Simulation Package (VASP 6.4.1).[41,42] Thermodynamic calculations employed the Perdew−Burke−Ernzerhof (PBE)[33] generalized gradient approximation (GGA) density functional and the projector augmented wave (PAW)[43,44] method, with a plane-wave energy cutoff of 520 eV and a Γ-centered $k$-point grid with a minimum spacing of 0.3 $Å^{-1}$. Convergence criteria were set to $3 \times 10^{-6}$ eV for electronic optimization and 0.03 $eV{\cdot}Å^{-1}$ for ionic relaxation. The electronic structures were computed with the r$^2$SCAN meta-generalized gradient approximation (meta-GGA) functional.[35]

For defect calculations in the dilute limit, we considered a $4 \times 4 \times 2$ supercell of $Li_2S$ as the pristine structure. Four Cu defect configurations were considered: (1) tetrahedral monovalent Cu represented by the reaction $32\ Li_2S + Cu_{Li}^{tet} \rightarrow Li_{63}Cu^{tet}S_{32} + Li$, (2) octahedral monovalent Cu with $32\ Li_2S + Cu_{Li}^{oct} + v_{Li}^{tet} \rightarrow Li_{63}Cu^{oct}S_{32} + Li$ (3) tetrahedral bivalent Cu with $32\ Li_2S + Cu_{Li}^{tet} + v_{Li}^{tet} \rightarrow Li_{62}Cu^{tet}S_{32} + 2\ Li$, and (4) octahedral bivalent Cu defect with $32\ Li_2S + Cu_{Li}^{oct} + 2v_{Li}^{tet} \rightarrow Li_{62}Cu^{oct}S_{32} + 2\ Li$. For the initial structure construction, Cu was introduced into the 32($Li_2S$) supercell, with Li removed to create vacancies as necessary. Given the 64 tetrahedral and 32 octahedral sites available for Cu and Li vacancies, we sampled several symmetrically distinct orderings using the StructureMatcher method as implemented in Pymatgen.[45] These ordered phases were then computed by DFT. The defect formation energy is defined as $\Delta E_{f,defect} = \Delta E_{product} - \Delta E_{reactant}$. For instance, $\Delta E_{f,defect} = E_{Li_{63}Cu^{+}S_{32}} + E_{Li} - 32E_{Li_2S} - E_{Cu}$ for tetrahedral monovalent Cu. The energies for Li and Cu were obtained using the same calculation procedure considering the ground-state polymorph of each elemental structure.

To identify the lowest-energy configuration of $Li_{1.7}Cu_{0.15}S$, we started from the unit cell structure obtained through X-ray diffraction (XRD) (Figure 2b) and extended it into a $4 \times 2 \times 2$ supercell (equivalent to a $4 \times 4 \times 4$ supercell of $Li_2S$). Various configurations of Li/Cu/vacancies on tetrahedral sites and Cu/vacancies on octahedral sites were systematically enumerated. These structures were then initialized and evaluated using DFT calculations, following the same computational settings described above. The internal energy, configurational entropy, and free energy change in $Li_{1.7}Cu_{0.15}S$ were calculated by the following formulations. The total reaction is given by $54Li_2S + 10CuS + 2Li \rightarrow Li_{110}Cu_{10}S_{64}$. The internal energy change is defined by $\Delta E_{rxn} = E_{Li_{110}Cu_{10}S_{64}} - 54E_{Li_2S} - 10E_{CuS} - 2E_{Li}$, where $E$ represents the internal energy obtained from DFT calculations. The configurational entropy was computed using the entropy of mixing formula $S_{config} = -Nk_B\sum_{i=1}^{r} x_i \ln x_i$, and the reaction entropy was then calculated by $\Delta S_{config} = S_{Li_{110}Cu_{10}S_{64}}$ (presuming that $Li_2S$, CuS, and Li have no configurational entropy). Finally, the free energy was determined by the Gibbs free energy relation $\Delta G_{rxn} = \Delta E_{rxn} - T\Delta S_{config}$.

Using the lowest-energy configuration of $Li_{110}Cu_{10}S_{64}$ identified through DFT calculations, ab initio molecular dynamics (AIMD) simulations were performed again using VASP and the PBE density functional. The simulations were performed under the *NVT* ensemble at a temperature of 800 K, regulated by the Nosé−Hoover thermostat,[46] with a time step of 1 fs. A single $k$-point (Γ-point) and a plane-wave energy cutoff of 400 eV were employed in the AIMD calculations. To achieve extended modeling of atomic-scale dynamics, we also used the universal machine learning interatomic potential CHGNet version 0.3.0.[34] CHGNet MD calculations were conducted using the *NVT* ensemble at 800 K as implemented in the Atomic Simulation Environment.[47] These simulations employed a 2 fs time step with the Berendsen inhomogeneous thermostat.

To analyze the local charge distribution, the Bader[48] charge analysis method and LOBSTER projected DOS/COHP[49] were applied. Pymatgen[45,51] was used for preparing and analyzing calculations and VESTA[50] was employed for structure visualization. Coordination analysis was performed using CrystalNN as implemented in pymatgen.[52]

## ■ ASSOCIATED CONTENT

### Supporting Information

The Supporting Information is available free of charge at https://pubs.acs.org/doi/10.1021/acs.chemmater.5c01328.

> Discharge and charge capacity of the all-solid-state batteries using $Li_{2-2x}Cu_xS$ cathode; ionic conductivity, ionic resistance, and electronic conductivity of $Li_{2-2x}Cu_xS$; fitting parameters of $Li_{2-2x}Cu_xS$ solid solution with different structure models; and temperature dependence of magnetic moments of $Li_{2-2x}Cu_xS$ electrodes (PDF)

### Accession Codes

Deposition Number 2452253 contains the supplementary crystallographic data for this paper. These data can be obtained free of charge via the joint Cambridge Crystallographic Data Centre (CCDC) and Fachinformationszentrum Karlsruhe Access Structures service.

## ■ AUTHOR INFORMATION


### Corresponding Authors

**Akira Miura** − *Faculty of Engineering, Hokkaido University, Sapporo 060-8628, Japan;* orcid.org/0000-0003-0388-9696; Email: amiura@eng.hokudai.ac.jp

**Christopher J. Bartel** − *Department of Chemical Engineering and Materials Science, University of Minnesota, Minneapolis, Minnesota 55455, United States;* orcid.org/0000-0002-5198-5036; Email: cbartel@umn.edu

### Authors

**Yi-Ting Cheng** − *Department of Chemical Engineering and Materials Science, University of Minnesota, Minneapolis, Minnesota 55455, United States;* orcid.org/0000-0002-1670-9933

**Takenaka Masahiro** − *Department of Chemistry of Functional Molecules, Konan University, Hyogo, Kobe 658-8501, Japan*

**Yusuke Nambu** − *Institute for Integrated Radiation and Nuclear Science, Kyoto University, Kumatori, Osaka 590-0494, Japan; FOREST, Japan Science and Technology Agency, Kawaguchi, Saitama 332-0012, Japan;* orcid.org/0000-0003-1167-7124

**Shunsuke Sasaki** − *Nantes Université, CNRS, Institut des Matériaux de Nantes Jean Rouxel, IMN, Nantes F-44000, France;* orcid.org/0000-0001-8358-1629

**Masanori Nagao** − *Center for Crystal Science and Technology, University of Yamanashi, Kofu, Yamanashi 400-0021, Japan;* orcid.org/0000-0002-1139-7838

**Takato Mitsudome** − *Department of Materials Engineering Science, Graduate School of Engineering Science, Osaka University, Toyonaka, Osaka 560-8531, Japan;* orcid.org/0000-0003-3071-8243

**Yuta Fujii** − *Faculty of Engineering, Hokkaido University, Sapporo 060-8628, Japan;* orcid.org/0000-0002-8381-4119

**Kiyoharu Tadanaga** − *Faculty of Engineering, Hokkaido University, Sapporo 060-8628, Japan;* orcid.org/0000-0002-3319-4353

**Nobuya Machida** − *Department of Chemistry of Functional Molecules, Konan University, Hyogo, Kobe 658-8501, Japan*

Complete contact information is available at: https://pubs.acs.org/10.1021/acs.chemmater.5c01328

### Notes

The authors declare no competing financial interest.

## ■ ACKNOWLEDGMENTS

A.M. is grateful to Ms. Masae Sawamoto for preparing the powder samples for the SXRD, ND, and magnetic measurements as well as Prof. Gerbrand Ceder for valuable feedback about the similarity of crystal structure between $Li_2S$−CuS and $BiF_3$. We would like to express our gratitude to Mr. Daisuke Yazeki, Instrumental Analysis and Open Facility Unit, Global Research Facility Alliance Center, Office for Integrated Technical Core Hub, Hokkaido University for performing ICP-OES using ICPE-9000 and providing insight and expertise that greatly assisted the research. This study was partially supported by JST Gtex (JPMJGX23S5, JPMJGX23S2), JST FOREST (JPMJFR202V), and JSPS KAKENHI (21H03732, 24K01578, JP24K17751, 22H05145, 24K00572). S.S. and A.M. thank the "PHC SAKURA" program supported bilaterally by JSPS (project number: JSJSBP12-2332-2) and French MEAE-MESR (project number: 49658ZH). Y.-T.C. and C.J.B. acknowledge support from the University of Minnesota in the form of new faculty start-up. The authors acknowledge the Minnesota Supercomputing Institute (MSI) at the University of Minnesota for providing resources that contributed to the research results reported within this paper.

## ■ REFERENCES

(1) Clément, R. J.; Lun, Z.; Ceder, G. Cation-disordered rocksalt transition metal oxides and oxyfluorides for high energy lithium-ion cathodes. *Energy Environ. Sci.* **2020**, *13* (2), 345−373.

(2) Liu, H.; Zhu, Z.; Yan, Q.; Yu, S.; He, X.; Chen, Y.; Zhang, R.; Ma, L.; Liu, T.; Li, M.; et al. A disordered rock salt anode for fast-charging lithium-ion batteries. *Nature* **2020**, *585* (7823), 63−67.

(3) Chen, Y.; Zhao, X.; Chen, K.; Koirala, K. P.; Giovine, R.; Yang, X.; Wang, S.; Szymanski, N. J.; Xiong, S.; Lun, Z.; et al. Coherent-Precipitation-Stabilized Phase Formation in Over-Stoichiometric Rocksalt-Type Li Superionic Conductors. *Adv. Mater.* **2025**, *37*, No. e2416342.

(4) Bruce, P. G.; Freunberger, S. A.; Hardwick, L. J.; Tarascon, J. M. Li-$O_2$ and Li-S batteries with high energy storage. *Nat. Mater.* **2012**, *11* (1), 19−29.

(5) Hayashi, A.; Ohtomo, T.; Mizuno, F.; Tadanaga, K.; Tatsumisago, M. All-solid-state Li/S batteries with highly conductive glass−ceramic electrolytes. *Electrochem. Commun.* **2003**, *5* (8), 701−705.

(6) Hakari, T.; Hayashi, A.; Tatsumisago, M. Li2S-Based Solid Solutions as Positive Electrodes with Full Utilization and Superlong Cycle Life in All-Solid-State Li/S Batteries. *Advanced Sustainable Systems* **2017**, *1* (6), No. 1700017.

(7) Wan, H.; Zhang, B.; Liu, S.; Zhang, J.; Yao, X.; Wang, C. Understanding LiI-LiBr Catalyst Activity for Solid State Li(2)S/S Reactions in an All-Solid-State Lithium Battery. *Nano Lett.* **2021**, *21* (19), 8488−8494.

(8) Fujita, Y.; Hakari, T.; Sakuda, A.; Deguchi, M.; Kawasaki, Y.; Tsukasaki, H.; Mori, S.; Tatsumisago, M.; Hayashi, A. $Li_2S$−LiI Solid Solutions with Ionic Conductive Domains for Enhanced All-Solid-State Li/S Batteries. *ACS Applied Energy Materials* **2022**, *5* (8), 9429−9436.

(9) Fujita, Y.; Sakuda, A.; Hasegawa, Y.; Deguchi, M.; Motohashi, K.; Jiong, D.; Tsukasaki, H.; Mori, S.; Tatsumisago, M.; Hayashi, A. High Capacity Li(2) S-Li(2) O-LiI Positive Electrodes with Nanoscale Ion-Conduction Pathways for All-Solid-State Li/S Batteries. *Small* **2023**, *19* (36), No. e2302179.

(10) Gao, J.; Gao, Y.; Hao, J.; Sun, X.; Zhao, F.; Zhang, Y.; Si, W.; Wu, J. Activating Redox Kinetics of $Li_2S$ via $Cu^+$, $I^-$ Co-Doping Toward High-Performance All-Solid-State Lithium Sulfide-Based Batteries. *Small* **2024**, *20* (47), No. e2404171.

(11) Sakuda, A.; Ohara, K.; Fukuda, K.; Nakanishi, K.; Kawaguchi, T.; Arai, H.; Uchimoto, Y.; Ohta, T.; Matsubara, E.; Ogumi, Z.; et al. Amorphous Metal Polysulfides: Electrode Materials with Unique Insertion/Extraction Reactions. *J. Am. Chem. Soc.* **2017**, *139* (26), 8796−8799.

(12) Fujii, Y.; Kobayashi, M.; Miura, A.; Rosero-Navarro, N. C.; Li, M.; Sun, J.; Kotobuki, M.; Lu, L.; Tadanaga, K. Fe−P−S electrodes for all-solid-state lithium secondary batteries using sulfide-based solid electrolytes. *J. Power Sources* **2020**, *449*, No. 227576.

(13) Hu, Y.; Sun, Z.; Zhang, Z.; Liu, S.; He, F.; Liu, Y.; Zhuang, Z.; Liu, F. Lithium-Rich Li2TiS3 Cathode Enables High-Energy Sulfide All-Solid-State Lithium Batteries. *Adv. Energy Mater.* **2023**, *13* (5), No. 2202756.

(14) Kwok, C. Y.; Xu, S.; Kochetkov, I.; Zhou, L.; Nazar, L. F. High-performance all-solid-state $Li_2S$ batteries using an interfacial redox mediator. *Energy Environ. Sci.* **2023**, *16* (2), 610−618.

(15) Kawasaki, Y.; Tsukasaki, H.; Ayama, T.; Mori, S.; Deguchi, M.; Tatsumisago, M.; Sakuda, A.; Hayashi, A. Synthesis and Electrochemical Properties of $Li_3CuS_2$ as a Positive Electrode Material for All-Solid-State Batteries. *ACS Applied Energy Materials* **2021**, *4* (1), 20−24.

(16) Gamo, H.; Hikima, K.; Matsuda, A. Transition-Metal Sulfides for High-Performance Lithium Sulfide Cathodes in All-Solid-State Lithium-Sulfur Batteries. *ACS Omega* **2023**, *8* (48), 45557−45565.

(17) Phuc, N. H. H.; Takaki, M.; Hiroyuki, M.; Atsunori, M. Preparation of $Li_{2-3x}Al_xS$ for All-Solid-State Li-S Battery. *Frontiers in Energy Research* **2021**, *8*, No. 606023.

(18) Phuc, N. H. H.; Takaki, M.; Kazuhiro, H.; Hiroyuki, M.; Atsunori, M. Dual effect of MgS addition on $Li_2S$ ionic conductivity and all-solid-state Li−S cell performance. *SN Applied Sciences* **2020**, *2* (11), 1−9.

(19) Fan, X.; Hu, E.; Ji, X.; Zhu, Y.; Han, F.; Hwang, S.; Liu, J.; Bak, S.; Ma, Z.; Gao, T.; Liou, S.-C.; Bai, J.; Yang, X.-Q.; Mo, Y.; Xu, K.; Su, D.; Wang, C. High energy-density and reversibility of iron fluoride cathode enabled via an intercalation-extrusion reaction. *Nat. Commun.* **2018**, *9*, 2324.

(20) Sears, V. F. Neutron scattering lengths and cross sections. *Neutron News* **1992**, *3* (3), 26−37.

(21) Wederni, A.; Daza, J.; Ben Mbarek, W.; Saurina, J.; Escoda, L.; Suñol, J.-J. Crystal Structure and Properties of Heusler Alloys: A Comprehensive Review. *Metals* **2024**, *14* (6), 688.

(22) Hund, F.; Fricke, R. Der Kristallbau von $\alpha$-$BiF_3$. *Zeitschrift für anorganische Chemie* **1949**, *258* (3−5), 198−204. (acccessed 2025/04/13)

(23) Buckley, A. N.; Skinner, W. M.; Harmer, S. L.; Pring, A.; Lamb, R. N.; Fan, L.-J.; Yang, Y.-w. Examination of the proposition that Cu(II) can be required for charge neutrality in a sulfide lattice — Cu in tetrahedrites and sphalerite. *Can. J. Chem.* **2007**, *85* (10), 767−781.

(24) Goh, S. W.; Buckley, A. N.; Lamb, R. N. Copper(II) sulfide? *Minerals Engineering* **2006**, *19* (2), 204−208.

(25) Jobic, S.; Brec, R.; Rouxel, J. Occurrence and characterization of anionic bondings in transition metal dichalcogenides. *J. Alloys Compd.* **1992**, *178* (1), 253−283.

(26) Sasaki, S.; Clarke, S. J.; Jobic, S.; Cario, L. Anionic Redox Topochemistry for Materials Design: Chalcogenides and Beyond. *ACS Organic & Inorganic Au* **2024**, *4* (1), 26−40.

(27) Mehrotra, P. K.; Hoffmann, R. Copper(I)-copper(I) interactions. Bonding relationships in d10-d10 systems. *Inorg. Chem.* **1978**, *17* (8), 2187−2189.

(28) Bodenez, V.; Dupont, L.; Laffont, L.; Armstrong, A. R.; Shaju, K. M.; Bruce, P. G.; Tarascon, J. M. The reaction of lithium with $CuCr_2S_4$—lithium intercalation and copper displacement/extrusion. *J. Mater. Chem.* **2007**, *17* (30), 3238−3247.

(29) Goodenough, J. B.; Kim, Y. Locating redox couples in the layered sulfides with application to $Cu[Cr_2]S_4$. *J. Solid State Chem.* **2009**, *182* (10), 2904−2911.



https://doi.org/10.1021/acs.chemmater.5c01328
*Chem. Mater.* 2025, 37, 8521−8528

(30) Li, D.; Bancroft, G. M.; Kasrai, M.; Fleet, M. E.; Feng, X. H.; Yang, B. X.; Tan, K. H. S K- and L-edge XANES and electronic structure of some copper sulfide minerals. *Phys. Chem. Miner.* **1994**, *21*, 317−324.
(31) Schultz, S.; Dunifer, G. Observation of Spin Waves in Sodium and Potassium. *Phys. Rev. Lett.* **1967**, *18* (8), 283−287.
(32) Sturza, M.; Han, F.; Shoemaker, D. P.; Malliakas, C. D.; Chung, D. Y.; Jin, H.; Freeman, A. J.; Kanatzidis, M. G. $NaBa_2Cu_3S_5$: A Doped p-Type Degenerate Semiconductor. *Inorg. Chem.* **2013**, *52* (12), 7210−7217.
(33) Perdew, J. P.; Burke, K.; Ernzerhof, M. Generalized Gradient Approximation Made Simple. *Phys. Rev. Lett.* **1996**, *77* (18), 3865−3868.
(34) Deng, B.; Zhong, P.; Jun, K.; Riebesell, J.; Han, K.; Bartel, C. J.; Ceder, G. CHGNet as a pretrained universal neural network potential for charge-informed atomistic modelling. *Nature Machine Intelligence* **2023**, *5* (9), 1031−1041.
(35) Furness, J. W.; Kaplan, A. D.; Ning, J.; Perdew, J. P.; Sun, J. Accurate and Numerically Efficient r2SCAN Meta-Generalized Gradient Approximation. *J. Phys. Chem. Lett.* **2020**, *11* (19), 8208−8215.
(36) Suekuni, K.; Lee, C. H.; Tanaka, H. I.; Nishibori, E.; Nakamura, A.; Kasai, H.; Mori, H.; Usui, H.; Ochi, M.; Hasegawa, T.; et al. Retreat from Stress: Rattling in a Planar Coordination. *Adv. Mater.* **2018**, *30* (13), No. e1706230.
(37) Maji, K.; Raveau, B.; Lemoine, P.; Boullay, P.; Acharyya, P.; Shen, X.; Renaud, A.; Pelletier, V.; Gautier, R.; Carnevali, V.; et al. Three-Fold Coordination of Copper in Sulfides: A Blockade for Hole Carrier Delocalization but a Driving Force for Ultralow Thermal Conductivity. *J. Am. Chem. Soc.* **2024**, *146* (14), 9741−9754.
(38) Kawaguchi, S.; Kobayashi, S.; Yamada, H.; Ashitani, H.; Takemoto, M.; Imai, Y.; Hatsui, T.; Sugimoto, K.; Sakata, O. High-throughput and high-resolution powder X-ray diffractometer consisting of six sets of 2D CdTe detectors with variable sample-to-detector distance and innovative automation system. *Journal of Synchrotron Radiation* **2024**, *31* (4), 955−967.
(39) Nambu, Y.; Ikeda, Y.; Taniguchi, T.; Ohkawara, M.; Avdeev, M.; Fujita, M. Neutron Powder Diffractometer HERMES — After the Decade-Long Shutdown. *J. Phys. Soc. Jpn.* **2024**, *93* (9), No. 091005.
(40) Coelho, A. A. TOPAS and TOPAS-Academic: an optimization program integrating computer algebra and crystallographic objects written in C++. *J. Appl. Crystallogr.* **2018**, *51* (1), 210−218.
(41) Kresse, G.; Furthmüller, J. Efficiency of ab-initio total energy calculations for metals and semiconductors using a plane-wave basis set. *Comput. Mater. Sci.* **1996**, *6* (1), 15−50.
(42) Kresse, G.; Furthmüller, J. Efficient iterative schemes for ab initio total-energy calculations using a plane-wave basis set. *Phys. Rev. B* **1996**, *54* (16), 11169−11186.
(43) Kresse, G.; Joubert, D. From ultrasoft pseudopotentials to the projector augmented-wave method. *Phys. Rev. B* **1999**, *59* (3), 1758−1775.
(44) Blöchl, P. E. Projector augmented-wave method. *Phys. Rev. B* **1994**, *50* (24), 17953−17979.
(45) Ong, S. P.; Richards, W. D.; Jain, A.; Hautier, G.; Kocher, M.; Cholia, S.; Gunter, D.; Chevrier, V. L.; Persson, K. A.; Ceder, G. Python Materials Genomics (pymatgen): A robust, open-source python library for materials analysis. *Comput. Mater. Sci.* **2013**, *68*, 314−319.
(46) Nosé, S. A unified formulation of the constant temperature molecular dynamics methods. *J. Chem. Phys.* **1984**, *81* (1), 511−519. (acccessed 2/13/2025)
(47) Hjorth Larsen, A.; Jorgen Mortensen, J.; Blomqvist, J.; Castelli, I. E.; Christensen, R.; Dulak, M.; Friis, J.; Groves, M. N.; Hammer, B.; Hargus, C.; et al. The atomic simulation environment-a Python library for working with atoms. *Journal of physics. Condensed matter: an Institute of Physics journal* **2017**, *29* (27), 273002.
(48) Henkelman, G.; Arnaldsson, A.; Jónsson, H. A fast and robust algorithm for Bader decomposition of charge density. *Comput. Mater. Sci.* **2006**, *36* (3), 354−360.
(49) Maintz, S.; Deringer, V. L.; Tchougreeff, A. L.; Dronskowski, R. LOBSTER: A tool to extract chemical bonding from plane-wave based DFT. *J. Comput. Chem.* **2016**, *37* (11), 1030−1035.
(50) Momma, K.; Izumi, F. VESTA 3 for three-dimensional visualization of crystal, volumetric and morphology data. *J. Appl. Crystallogr.* **2011**, *44* (6), 1272−1276.
(51) George, J.; Petretto, G.; Naik, A.; Esters, M.; Jackson, A. J.; Nelson, R.; Dronskowski, R. G.-M.; Rignanese, G. H. Automated Bonding Analysis with Crystal Orbital Hamilton Populations. *ChemPlusChem* **2022**, No. e202200123.
(52) Pan, H.; Ganose, A. M.; Horton, M.; Aykol, M.; Persson, K. A.; Zimmermann, N. E. R.; Jain, A. Benchmarking Coordination Number Prediction Algorithms on Inorganic Crystal Structures. *Inorg. Chem.* **2021**, *60* (3), 1590−1603.




https://doi.org/10.1021/acs.chemmater.5c01328
Chem. Mater. 2025, 37, 8521−8528